Thrust Stand for Electric Propulsion Performance Evaulation

Kurt A. Polzin,* Thomas E. Markusic, Boris J. Stanojev, Amado Dehoyos, and Benjamin Spaun

NASA-Marshall Space Flight Center
Huntsville, AL 35812

An electric propulsion thrust stand capable of supporting testing of thrusters having a total mass of up to 125 kg and producing thrust levels between 100 μN to 1 N has been developed and tested. The design features a conventional hanging pendulum arm attached to a balance mechanism that converts horizontal deflections produced by the operating thruster into amplified vertical motion of a secondary arm. The level of amplification is changed through adjustment of the location of one of the pivot points linking the system. Response of the system depends on the relative magnitudes of the restoring moments applied by the displaced thruster mass and the twisting torsional pivots connecting the members of the balance mechanism. Displacement is measured using a non-contact, optical linear gap displacement transducer and balance oscillatory motion is attenuated using a passive, eddy-current damper. The thrust stand employs an automated leveling and thermal control system. Pools of liquid gallium are used to deliver power to the thruster without using solid wire conenctions, which can exert undesirable time-varying forces on the balance. These systems serve to eliminate sources of "zero-drift" that can occur as the stand thermally or mechanically shifts during the course of an experiment. An in-situ calibration rig allows for steady-state calibration before, during and after thruster operation. Thrust measurements were carried out on a cylindrical Hall thruster that produces mN-level thrust. The measurements were very repeatable, producing results that compare favorably with previously published performance data, but with considerably smaller uncertainty.

PACS numbers:

I. INTRODUCTION

Electric propulsion (EP) systems provide high specific impulse, but low thrust, relative to chemical propulsion systems. While chemical rocket thrust is generally measured using load cells[1], the low thrust levels associated with EP devices lead to thrust stands which more closely resemble sensitive laboratory mass scales, where physical displacement of one of the mechanical members in the balance system is used to infer the applied force. These balances are typically configured as either a hanging, inverted or torsional pendulum with the thruster mounted at the end of the pendulum arm.

The conventional hanging pendulum is the most simple of the three configurations and is highly stable when subjected to external perturbations. However, high sensitivity can only be attained with a long pendulum arm, which may be impractical if the test facility (vacuum chamber) is small. Therefore, conventional hanging pendulum thrust stands have been primarily used to test high thrust-to-weight, T/W, EP devices such as electrothermal arcjets and microwave electrothermal thrusters[2, 3]. Also, the displacement sensor is typically mounted on a separate reference structure that can (undesirably) move, independent of the pendulum mounting structure, and produce erroneous results.

Inverted pendulum thrust stands are less stable but

possess a greater sensitivity relative to the hanging pendulum configuration. They have been widely implemented to measure the performance of thrusters over a broad range of T/W, including resistojets, electrothermal arcjets, MPD thrusters[4–6], Hall thrusters[7–9], and ion thrusters. A problem for the inverted pendulum configuration is that its stability is a strong function of the stiffness of the (supporting) flexures, which can change during the course of a test due to, for example, heating.

Unlike both the conventional and inverted pendulum configurations, the restoring force in the torsional pendulum configuration (which rotates about an axis that is parallel to the gravity vector) can be made independent of the thruster mass. Consequently, torsional pendulum thrust stands provide the highest sensitivity, and have recently been implemented in micropropulsion performance evaluation[10–16]. They have also been shown to be effective in measuring the performance of pulsed thrusters[17–20]. The primary disadvantages of the torsional pendulum configuration are that the horizontal, asymmetric arrangement of its members can be difficult to configure within a vacuum chamber possessing limited space and its sensitivity does not readily allow for testing of higher power thrusters.

We describe in this work a new thrust stand design: the Variable Amplitude Hanging Pendulum with Extended Range (VAHPER)[21]. This thrust stand is a variant of the conventional pendulum, but it incorporates many novel features designed to enhance the quality of thrust data and the range of devices that can be tested. Specifically, the VAHPER thrust stand was designed to en-

---
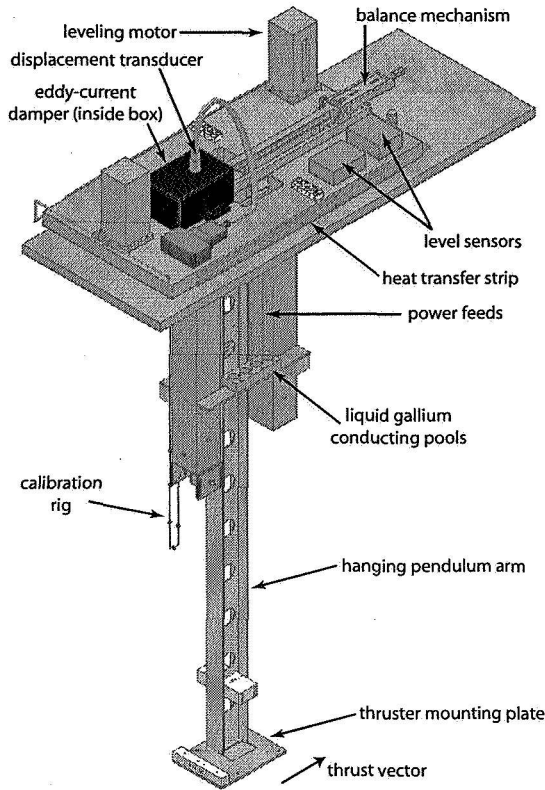
*Corresponding Author: Kurt.A.Polzin@nasa.gov

FIG. 1: Schematic illustration of the assembled VAHPER thrust stand.

described in this paper. Data demonstrating the sensitivity and thrust measurement capabilities of the VAHPER thrust stand are presented in section IV

II. VAHPER SYSTEM OVERVIEW

A schematic illustration of the VAHPER thrust stand is shown in Fig. 1. In the rest of this section, we describe in detail the various subsystems and the enhancement each component adds to the fidelity of the thrust measurement.

A. Balance Mechanism

The system of linkages comprising the VAHPER thrust stand balance mechanism are represented as a simplified schematic in Fig. 2. All of the pivots (points B,C,D,E) utilize frictionless torsional flexures manufactured by the C-Flex Bearing Corp. Member ABC pivots rigidly about point B while member DEF pivots about point E. Rotation of the two members are coupled through linkage CD. Unless otherwise noted, displacements are represented by the vector d_{ij}, member lengths by l_{ij} and angles by θ_{ijk} where i, j, and k are the endpoints.

Application of thrust T causes members ABC and DEF to rotate through angles α_1 and α_2, respectively, to the new position indicated by the primed (') points. In this configuration, horizontal deflection $d_{AA'}$ is con-

able thrust measurement of electric thrusters weighing between 1-125 kg and producing thrust levels from 1 mN to over 1 N. This is accomplished through a mechanical linkage system that translates horizontal displacement into amplified vertical displacement. The system provides for adjustable sensitivity though the adjustment of a single member. Displacement monitoring is performed on the vertically displaced member, which eliminates the need for a separate reference structure.

Pendulum-based thrust balances are susceptible to 'zero-drift', which means that when the thruster is turned off, the pendulum arm does not return to its initial position. Several components and subsystems have been included in the VAHPER thrust stand design to mitigate the causes of zero-drift. These include low friction flexural pivot mounts, a non-contact ratiometric position sensor, an on-board level control system, a thermal management system and an innovative method to feed power onto the thrust stand arm using liquid gallium pools.

In the next section we provide details regarding the design of the thrust stand. Section III contains information about the thruster and facility used for the experiments
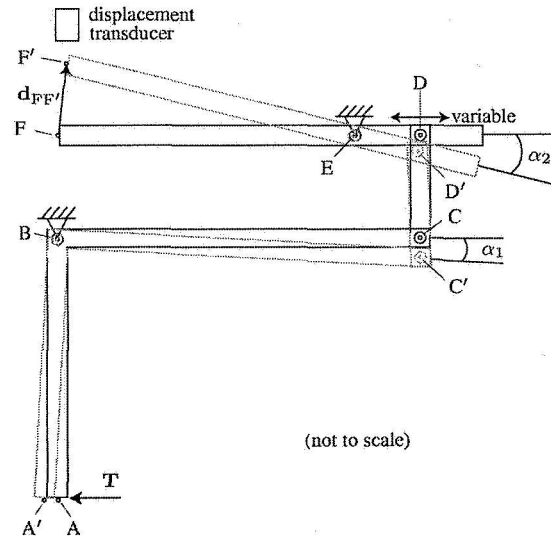

FIG. 2: Schematic illustration of the balance mechanism components in their undeflected and deflected positions (deflected beam positions shown in grey).

2

verted to (amplified) vertical deflection $d_{FF'}$, which is measured by the displacement transducer at the end of beam DEF. The VAHPER thrust stand pivots are mounted to the same structure as the displacement transducer, thus eliminating the need for a separate (and problematic) reference structure. The trigonometric exercise of relating $d_{AA'}$ to $d_{FF'}$ is performed in Appendix 1 and results in the equation set

$$\alpha_1 = 2\sin^{-1}\left(\frac{|d_{AA'}|}{2\,l_{AB}}\right), \quad |d_{FF'}| = 2\,l_{EF}\sin\left(\frac{\alpha_2}{2}\right),$$

$$\alpha_2 = \alpha_1 + \theta_{BC'D'} + \theta_{C'D'E} - \theta_{BCD} - \theta_{CDE}, \qquad (1)$$

where all the lengths and angles are known in terms of the initial geometric configuration and are defined in Appendix 1. The coordinates of the endpoints in the VAHPER thrust balance are given in Table I. Given this geometry, the amount of displacement amplification ($|d_{FF'}| / |d_{AA'}|$) realized in the system is plotted in in Fig. 3 as a function of the variable length l_{DE}.

To find the amount of actual deflection $|d_{FF'}|$ realized for a given level of thrust, we must perform a free body analysis of the various members, taking into account the

TABLE I: Coordinates of the undeflected points comprising the VAHPER thrust stand as shown in Fig. 2.

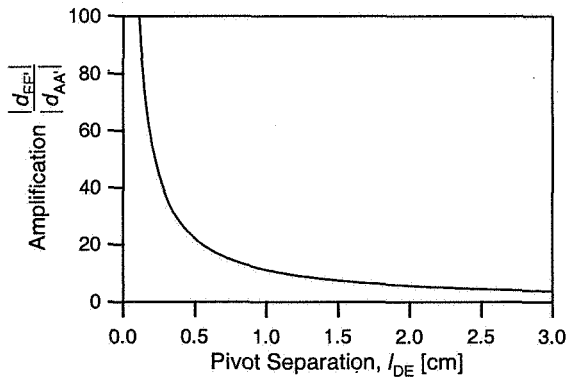|	x [cm]	y [cm]
A	0.0	-121.9
B	0.0	0.0
C	31.4	-3.2
D	0.5 to 3.0	4.2
E	30.4	4.2
F	-12.9	4.2

FIG. 3: Displacement amplification in the VAHPER thrust balance as a function of the variable length l_{DE}.

TABLE II: Spring constants for the torsional pivots in the VAHPER thrust stand.

	Spring Constant [cm-N/rad]
k_B	153.4
k_C	4.21
k_D	4.21
k_E	8.42

restoring moments exerted by the torsional flextures and the mass of the thruster (located at point A). This analysis is found in Appendix 2 and results in an expression relating the thrust $|T|$ to the angle α_1:

$$T = (M_B + M_{C'})/l_{AB} + m\,g\sin(\alpha_1)$$
$$+ \frac{(M_E + M_{D'})\,l_{BC}\cos\left(\frac{\pi}{2} - \theta_{BC'D'}\right)}{l_{AB}\,l_{DE}\cos\left(\frac{\pi}{2} - \theta_{C'D'E}\right)}. \qquad (2)$$

where the torsional pivot reaction moments M are defined in Eqs. (A12) with spring constants given in Table II. After the variable length l_{DE} is fixed, every term on the right hand side of the equation is a function of only α_1. The problem is most easily solved by iteratively varying α_1 until Eq. (2) equals a given thrust level. Equations (1) can then be used to find the member deflections in the system. In Fig. 4A we have plotted the predicted deflection at point F as a function of l_{DE} for a thruster having a mass of 5 kg and producing a fixed thrust of 10 mN. The same type of plot is shown in Fig. 4B for the case where a 40 kg thruster produces a constant 20 mN of thrust.

From Fig. 4, we see that even though the displacement amplification increases rapidly with decreasing l_{DE}, the actual deflection produced at point F by a given thrust level does not necessarily increase over the same range of l_{DE} but, rather, an optimal value exists for a given thruster and choice of springs. The reason for this is clearly illustrated in Fig. 4A, where moments exerted by the torsional pivots in response to the motion induced by the thruster begin to dominate the thrust stand's response as we decrease l_{DE} below 1.5 cm. Even in Fig. 4B where the thruster is significantly heavier, we observe the deflection curve beginning to peak as l_{DE} approaches 5 mm, indicating that the restoring forces in the system arising from the reactions of the torsional pivots are beginning approach the same level as the restoring force applied by the thruster's mass. While in this paper we only focus on cases that are representative of the existing VAHPER thrust stand hardware, a parametric analysis using Eqs. (1) and (2) could be performed to determine the global sensitivity of the curves in Fig. 4 to the various member lengths and spring constant values.
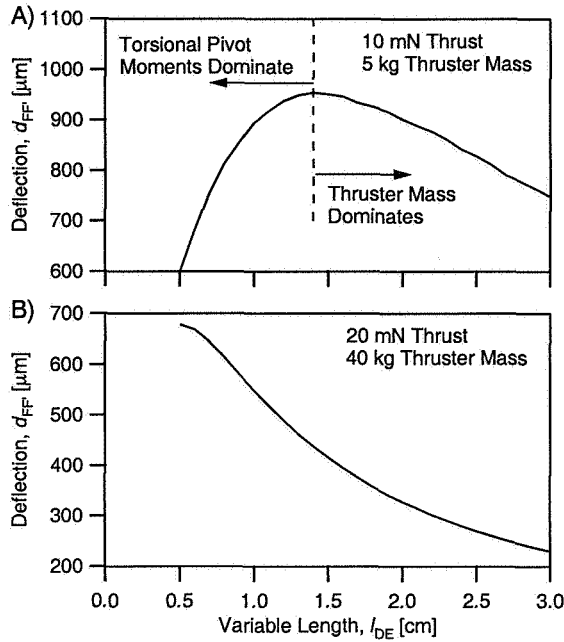
FIG. 4: Predicted deflection, $|d_{FF'}|$, as a function of the variable length l_{DE} for A) a 5 kg thruster producing 10 mN of thrust and B) a 40 kg thruster producing 20 mN of thrust (spring constant values from Table II are assumed in both cases).
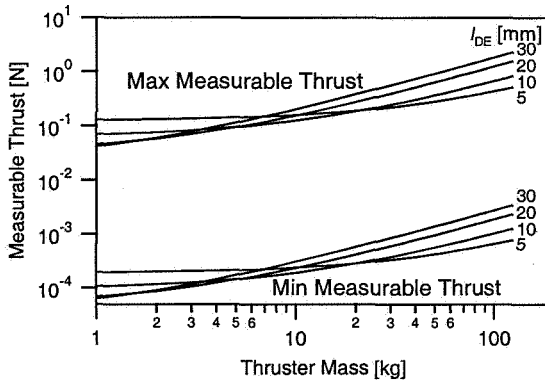

FIG. 5: Minimum and maximum measurable thrust levels on the VAHPER stand as a function of thruster mass and the variable length l_{DE}. The minimum and maximum levels correspond to deflections at point F of 13 μm and 8.5 mm, respectivley (spring constant values from Table II are assumed in both cases).

B. Displacement Sensing

Measurement of the distance $|d_{FF'}|$ is achieved using a BEI Precision Systems Linear Gap Displacement Transducer (LGDT), which is a non-intrusive (not in physical contact with member DEF) optical transducer that is relatively immune to external electric, radio frequency (RF), and magnetic interference. The LGDT illuminates the target surface with an IR LED through a concentric-ring fiber-optic probe. Light reflected from the target is analyzed using a ratiometric technique to derive the distance to the target surface. The analog voltage output of the LGDT varies linearly with the distance from the target to the tip of the probe.

The LGDT used on the VAHPER thrust stand has a resolution of 1.3 μm, a sensitivity of 0.75 mV/μm, and a 1% linear range of 8.5 mm. The sensor output is transmitted through a single, shielded twisted pair to a 12-bit A/D converter (NI PXI-1601). This conversion brings the overall resolution of the system to about 13 μm. Taking this as the minimum measurable distance $|d_{FF'}|$ and 8.5 mm as the maximum, and using Eq. (2), we can solve for the minimum and maximum resolvable thrust levels as a function of thruster mass and the variable length l_{DE}. These bounds are plotted in Fig. 5 for the VAHPER stand. We observe that for low thruster masses where the reactions of the torsional pivots dominate the thrust stand response, the minimum resolvable thrust is measured when the stand in in the configuration yielding the smallest displacement amplification (greatest value of l_{DE}). In addition, the greatest measurable thrust level is obtainable in the configuration yielding the largest displacement amplification (smallest value of l_{DE}). However, as thruster mass is increased, this counterintuitive trend reverses and the configuration yielding the greatest displacement amplification allows for measurement of the minimum resolvable thrust levels while the configuration giving minimal displacement amplification should be employed to measure the maximum resolvable thrust.

C. Damping

Attenuation of mechanical oscillations in the motion of the thrust balance is achieved using a passive, eddy-current damper. The damper is located at the end of the balance secondary beam, near the displacement sensor (see Fig. 1). The damper assembly is pictured in Fig. 6 and is comprised of four 3/8"-diameter samarium-cobalt permanent magnets embedded in a soft iron yoke. Opposing magnets are separated by a 1/8" slot, providing a magnetic field strength in the gap of ~0.2 T. A 1/16"-thick copper plate, attached to the end of the secondary beam, extends into the slot between the permanent mag-
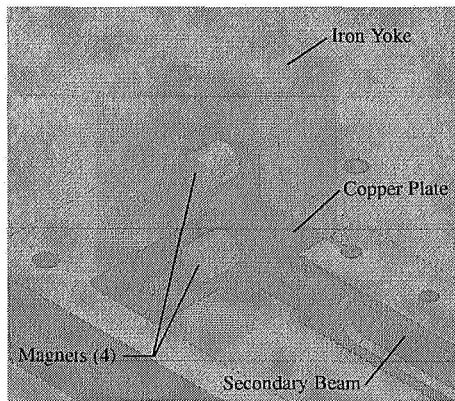
FIG. 6: Eddy-current oscillation damper illustration (note: iron yoke rendered transparent to reveal inner detail).

nets. Vertical motion of the secondary beam causes the copper plate to move relative to the applied magnetic field, inducing eddy-currents in the copper that dissipate the mechanical energy and provide near critical damping of thrust stand oscillations. The amount of dissipation can be adjusted either by adjusting the magnetic field strength or by changing the size or material of the moving plate to alter the exposed area or conductivity, respectively.

D.   Level Control

Zero drift of the displacement sensor signal is a ubiquitous problem in thrust measurement systems, deriving primarily from unsteady thermal loads and vacuum tank distortion during the course of a test. We have included a level control system in the VAHPER thrust stand design, to both sense and counteract deflections of the structure that supports the balance mechanism, with the aim of minimizing the zero drift during tests.

Level sensing is performed using a pair of high accuracy Jewell Instruments inclinometers with 0.001^o of accuracy over their full scale range of $\pm 3^o$ relative the the Earth's gravity vector. The sensors are mounted to the baseplate (see Fig. 1) perpendicular to each other to allow for two-axis (X, Y) detection. Any deviation from 0° (or any other user defined angle) causes the control system to adjust the baseplate position. The adjustments are performed by two high resolution (1 μm/step) four-phase stepper motors, which change the position of the baseplate until the inclinometers indicate that the baseplate is level.

E.   Thermal Management

A closed-loop thermal management system was implemented, with the goal of maintaining a constant balance temperature during tests, in order to minimize displacement zero drift. The balance mechanism is mounted on a thick (1.5"), water-cooled aluminum plate (see Fig. 1) to provide high thermal inertia. The water temperature is maintained at a constant temperature by a Thermo Neslab M150 programmable water chiller, which is capable of removing up to 5 kW of heat power. Temperature is measured on the thrust stand at various locations by thermocouples.

F.   Thruster Power Feeds

In many thrust measurements, the wires leading to the thruster can greatly affect the level of zero drift experienced over the course of a test. The wires experience Joule heating, causing them to deform during thruster operation (especially at high current levels like those used to pre-heat an emitter cathode), which can apply time-varying forces and torques to the thrust stand arm. In the VAHPER thrust stand design, this source of drift is eliminated by conducting current onto the thrust stand arm through pools of liquid gallium. Since the wires on the arm are only in contact with the liquid metal, they are unable to apply loads to the thrust stand arm.

G.   In-Situ Calibration

Displacement (thrust) calibration was accomplished by applying a series of known loads normal to the pendulum arm, and recording the resulting displacement measured at point F. A set of five known masses is attached at regular intervals along a Kevlar string (see Fig. 1). The string is wound around a spool and attached to a stepper motor, which allows for remote actuation of the calibration procedure. The bottom end of the string is draped over a low-friction pulley and attached to the hanging pendulum arm. As the weights are lowered, the string-mass-pulley system transfers the gravitational force on the weights to the thrust stand, normal to the pendulum arm. The calibration procedure is automated so that at any time (before, during or after a thrust measurement), the calibration weights can be lowered and retracted to provide continuous checks on the displacement calibration.
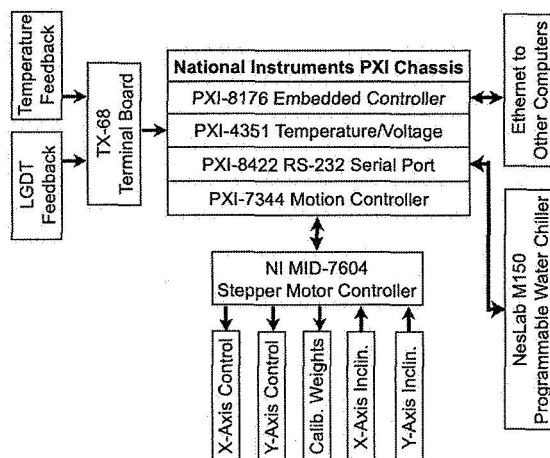
FIG. 7: VAHPER thrust stand control system architecture and data flow.

FIG. 8: A) Schematic illustration and B) photograph of the PPPL cylindrical Hall thruster.

1-10 mN.

H. Data Acquisition and Control

The control system and data flow are shown schematically in Fig. 7. The system architecture is based around a *National Instruments PXI-8176* embedded computer, which is mounted in a chassis along with several other modules that allow for communication with and control of various subsystems. Temperature and displacement data (in the form of a voltage signal) are brought into the system through a TX-68 terminal board. The stepper motors are controlled and by the MID-7604 module, which also receives feedback data from the inclinometers. Two-way communication with the programmable water chiller is performed through an RS-232 connection. By communicating with other PCs thought an Ethernet connection, a common time stamp can be established. This ability allows for all data to be tagged with the same time stamp, regardless of which computer is acquiring data. This is critical in the post analysis phase when thruster data (current, voltage, mass flow rate), which is controlled by a separate system, is cross-referenced and correlated with thrust stand deflection.

III. EXPERIMENTAL SETUP

We conducted experiments using a low-power ($\mathcal{O}(100)$ W) cylindrical Hall thruster to test the ability to resolve thrust levels on the lower end of the predicted thrust stand range. For the purpose of validation, a thruster was chosen for which thrust stand measurements from another facility already existed. Based on those measurements, we expected thrust levels between
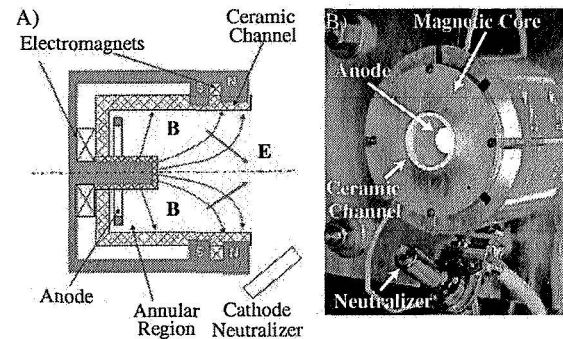
A. Vacuum Facility

The thrust stand is mounted inside a 9-ft diameter, 25-ft long stainless steel vacuum chamber. The vacuum level inside the chamber is maintained by two 2400 l/s turbopumps and two 9500 l/s cryopumps. The base pressure was 5.7×10^{-7} Torr and the background pressure of xenon during thruster operation at $\sim$5 sccm total flow rate was $\sim 9 \times 10^{-6}$ Torr.

B. Cylindrical Hall Thruster

The Princeton Plasma Physics Laboratory (PPPL) 3 cm cylindrical Hall thruster (CHT) was used for these experiments. A The CHT is illustrated schematically in Fig. 8A, while a photograph is shown in Fig. 8B. The Boron-Nitride thruster channel is a composite of a shorter, annular region and a longer, cylindrical region. Gas is injected through holes in the annular anode. The magnetic circuit consists of a magnetic core and two electromagnet coils that can be operated using independently controlled power supplies. More details on the CHT can be found in Refs. [22–26] and the references therein.

The working propellant for these experiments was research grade xenon gas. The cathode and anode flowrates were independently controlled using two MKS 0-10 sccm flow controllers (calibrated on Xe). A commercial HeatWave plasma source was used as the cathode neutralizer. In all our experiments, the cathode flowrate was 1 sccm.

IV. EXPERIMENTAL RESULTS

A. Thrust Stand Calibration

Displacement (thrust) calibration of the VAHPER thrust stand is accomplished using an in-situ calibration rig discussed in the previous section. A displacement waveform, as shown in Fig. 9A, is obtained by applying a series of known loads normal to the pendulum arm. The stability in the displacement zero is evident as the stand returns to its initial position roughly 14 minutes after we initiate the calibration procedure.

Calibration measurements and the resulting fit to the data set are plotted in Fig. 9B. An automated data reduction routine is used to analyze the displacement data and generate the curve fit coefficients which can be used to compute thrust. This analysis is performed under the assumption that the relationship between the applied force and the measured displacement is linear. The error propagation algorithm, which perform a linear curve fit of the data taking into account the error bars on the individual force and displacement measurements, is discussed in Ref. [27]. Based on the curve fit, we see that the ultimate resolution without the thruster running is ~50 μN.

B. Raw Thrust Data

The output of the LGDT, power supplies and mass flow controllers are recorded throughout the duration of the test. Raw data output by the LGDT is displayed in Fig. 10 for two separate CHT discharge voltages. We immediately see from this figure that there is very little zero-drift in the thrust balance position over this time period. Typically, the largest zero-drifts in past experiments have occurred between the time when the cathode heater is turned on and the discharge is ignited. This is due to the large current level needed to heat the cathode to thermionically emitting temperatures (23 A for our Heat-Wave cathode). We see in the VAHPER thrust stand data that there is no significant drift associated with cathode heater operation, thus validating our liquid metal power conduction scheme.

Prior to thrust measurements, the thruster is operated for approximately 30 minutes to condition the insulating surfaces in the discharge chamber. Thruster operation begins when the emitter cathode becomes hot enough to sustain a thermionic discharge. At this point, the discharge voltage is applied between the cathode and the anode. After the main discharge is activated, the magnetic field coils are energized and adjusted to the desired current levels. As expected, we observe fluctuations in the raw data trace as the field is adjusted to the final value since the actual thrust varies as the B-field is adjusted.
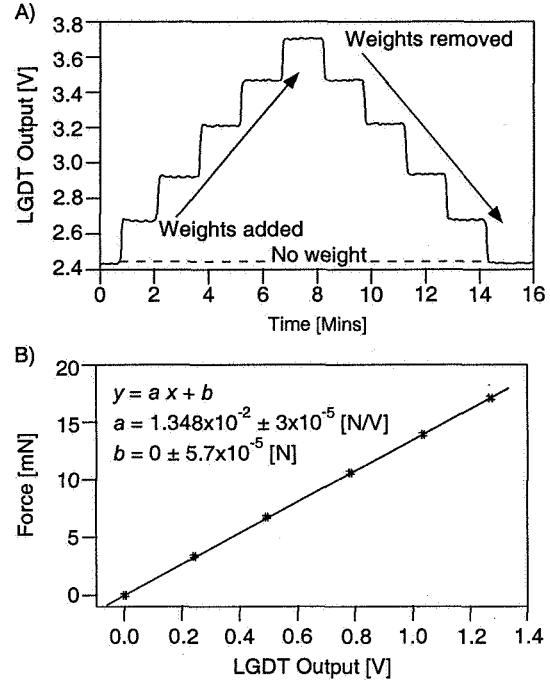

FIG. 9: A) Time history of VAHPER calibration data showing LGDT measured output as the calibration weights were added and removed. B) Applied calibration force plotted as a function of LGDT response. The linear curve is a fit to the displayed data. Error bars on the datapoints and the fit coefficients represent a 68% (1σ) confidence interval.

Once the field is set, no further adjustments are made, allowing for a 1.5-2 minute steady-state period. After this time period, the discharge is extinguished and the field coils are deenergized in preparation for the next test. We allow enough time between thruster operating points to re-establish the LGDT output baseline (zero level).

C. Thruster Performance Measurements

The thrust (T) is found by first finding the LGDT output voltage difference between the steady-state portion of thruster operation and the zero level output immediately following thruster shutdown (see Fig. 10). These data are then converted to thrust using the calibration curve-fit constants found in Fig. 9B. Specific impulse (I_{sp}) and anode efficiency (η) are defined as

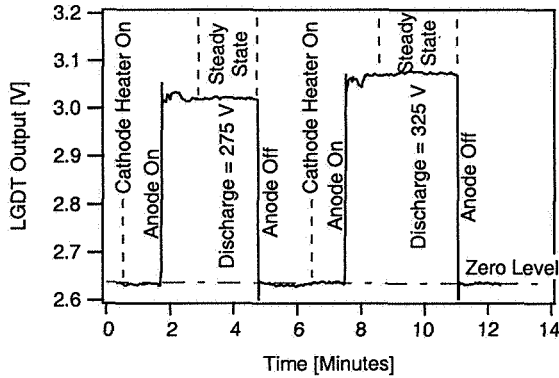$$I_{sp} = \frac{T}{\dot{m}g_0}, \quad \eta = \frac{T^2}{2\dot{m}P},$$

7

FIG. 10: Raw LGDT output data as a function of elapsed time for two thruster operating points.

FIG. 11: Performance measurements for a 3 cm cylindrical Hall thruster: A) Thrust, B) I_{sp}, C) Anode Efficiency as a function of discharge power. The error bars represent a 95% (2σ) confidence interval. No error bars are displayed on the data from Ref. [28].

where P is the discharge power and $\dot{m}$ is the mass flow rate through the anode. The uncertainty levels on the performance data represent a 95% (2σ) confidence interval.

Thrust measurements corresponding to an anode mass flow rate of 3.9 sccm are presented in Fig. 11A, with the corresponding I_{sp} values found in Fig. 11B and the anode efficiencies plotted in Fig. 11C. Our data span a range between 130 to 185 W in discharge power, with resulting thrust levels between 4.8 and 6.2 mN, I_{sp} levels between 1275 and 1650 s, and anode efficiencies from 23 to 27%. Also plotted in this figure are measurements from Ref. [28] performed at Princeton University on a swinging-gate style thrust stand using the same thruster. The agreement between this data set and our data is very good, and the error bars on our data are ~20% of those associated with the measurements performed at Princeton.

V. CONCLUSIONS

We have developed a hanging pendulum thrust stand, which employs an adjustable mechanical linkage system to convert the horizontal deflection of the pendulum arm to amplified vertical deflection of a secondary beam. Furthermore, the geometry allows for mounting of the secondary beam and the deflection measurement system to the same baseplate, eliminating the need to perform measurements of deflection at the end of the pendulum using a separate reference structure. Deflection amplification is a function of geometry, and depends only on the variable length l_{DE}. The system's response, on the other hand, depends on the relative magnitudes of the moments applied to the system by the displaced thruster mass and the deflected torsional pivots. The thrust stand is capable of
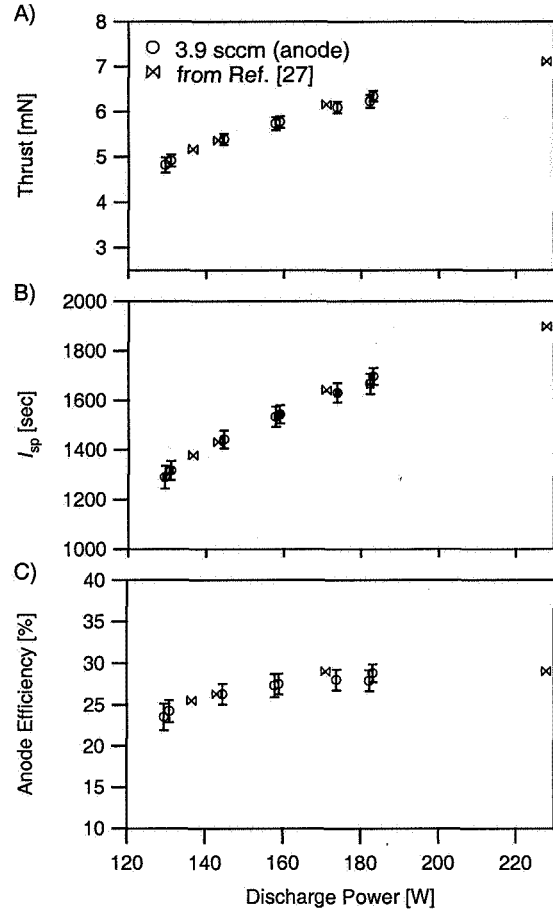
measuring thrust levels ranging from 100 μN to 1 N, and can support thrusters of up to 125 kg total mass.

Several supporting systems have been implemented to enhance the measurement accuracy: high-sensitivity, non-contact displacement sensing, an automated leveling system, an oscillation damping device, thermal control, and a novel means to deliver power to the thruster. These subsystems serve to eliminate the sources of zero-drift. In addition, an in-situ calibration rig enables displacement calibration at any time during a test.

Experiments using a well-characterized thruster validated the capability of the thrust stand to measure thrust, especially at low thrust levels. Our data were in good agreement with a data set obtained using a different,

well-characterized thrust stand, the error bars on our data set were only 20% of those found in the literature, demonstrating the effectiveness of the systems listed in the previous paragraph.

APPENDIX: THEORETICAL ANALYSIS OF BALANCE MECHANISM

We proceed with a derivation of Eqs. 1 and 2 from first principles. Scalar quantities of the displacement vectors $\mathbf{d}_{ij}$ are represented by d_{ij}. All endpoints and vectors are the same as those defined in Fig. 2.

1. Balance Mechansim Deflection Analysis

To find the displacement amplification, we must relate the displacements $d_{FF'}$ and $d_{AA'}$. From Figs. 12A and 12B we see that isosceles triangles AA'B and EFF' are used to write the displacements in terms of the angles α_1 and α_2:

$$\alpha_1 = 2\sin^{-1}\left(\frac{d_{AA'}}{2\,l_{AB}}\right), \quad (A1)$$

$$d_{FF'} = 2\,l_{EF}\sin\left(\frac{\alpha_2}{2}\right). \quad (A2)$$

Writing an equation relating $d_{FF'}$ and $d_{AA'}$ now comes down to an exercise in writing α_2 in terms of α_1.

Once the length l_{DE} is chosen, the initial separation distances and angles within the linkage mechanism are fully known. The bulk of our analysis will focus on the quadrilateral BCDE shown in its undeflected position in Fig. 12C. When the mechanism is deflected as shown in Fig. 12D, we can write (see Fig. 2)

$$\theta_{EBC'} = \theta_{EBC} + \alpha_1, \quad (A3)$$

$$\theta_{D'EB} = \theta_{DEB} - \alpha_2. \quad (A4)$$

The length $l_{C'E}$ is written using the law of cosines as:

$$l_{C'E} = \left(l_{BC}^2 + l_{BE}^2 - 2\,l_{BC}\,l_{BE}\cos\left(\theta_{EBC} + \alpha_1\right)\right)^{1/2}. \quad (A5)$$

With all the lengths in the triangles BC'E and C'D'E known, we again use the law of cosines to write:

$$\theta_{BC'D'} = \cos^{-1}\left(\frac{l_{BC}^2 + l_{C'E}^2 - l_{BE}^2}{2\,l_{BC}\,l_{C'E}}\right) + \cos^{-1}\left(\frac{l_{C'E}^2 + l_{CD}^2 - l_{DE}^2}{2\,l_{C'E}\,l_{CD}}\right), \quad (A6)$$

$$\theta_{C'D'E} = \cos^{-1}\left(\frac{l_{DE}^2 + l_{CD}^2 - l_{C'E}^2}{2\,l_{DE}\,l_{CD}}\right). \quad (A7)$$

The geometry is such that the angles comprising quadrilaterals BCDE and BC'D'E must both sum to 2π radians. If we equate the angles from the two quadrilaterals, substitute for the angles in BC'D'E using Eqs. (A3) and (A4), and rearrange the terms, we obtain

$$\alpha_2 = \alpha_1 + \theta_{BC'D'} + \theta_{C'D'E} - \theta_{BCD} - \theta_{CDE}. \quad (A8)$$

Given an initial geometry and selecting a value for α_1, all the angles on the right-hand side of Eq. (A8) are known. Equations (A1), (A2) and (A8) allow us to relate $d_{AA'}$ to $d_{FF'}$ and are exactly those given as Eqs. (1).

2. Linkage Response to Applied Thrust

An operating thruster applies a force $\mathbf{T}$ to the thrust stand, deflecting the linkages to a new position denoted by primes (') in Fig. 2. This motion is opposed by the torque arising from the weight of the thruster, mg, and
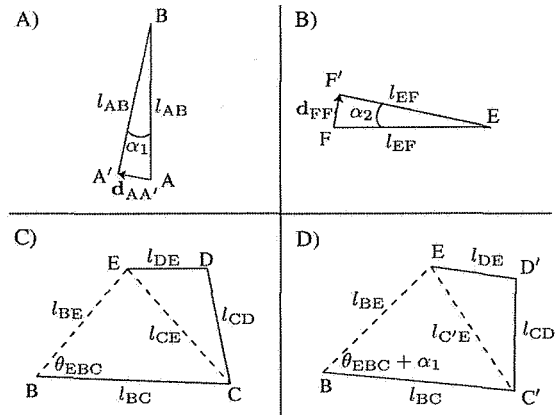

FIG. 12: Schematic illustrations (not to scale) of various members in the VAHPER thrust balance. The endpoints, vectors and lengths are the same as those defined in Fig. 2.
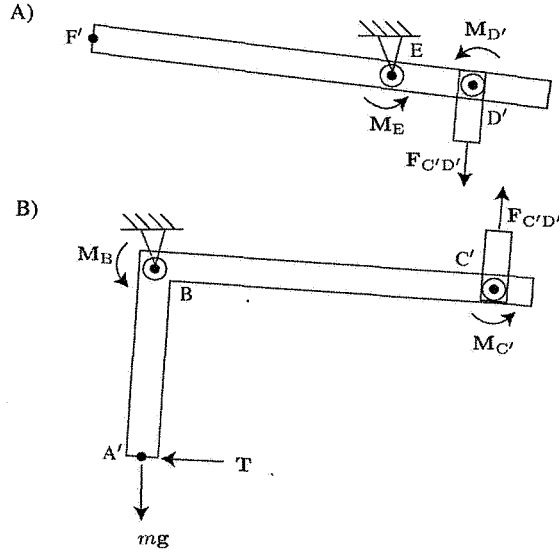
A)

B)

FIG. 13: Free body diagrams (not to scale) showing the relevant forces and torsional spring moments applied to the (A) upper and (B) lower linkages in the VAHPER thrust balance when the system is deflected. The deflected positions are defined in Fig. 2.

by the moments produced as the torsional springs flex from their neutral positions. To find the actual deflection $d_{AA'}$ we must sum the moments applied to each linkage.

Free body diagrams showing the moments applied by deflected torsional springs and external forces applying

additional moments to both the upper and lower linkages are shown in Fig. 13. In the static case, summing the moments for linkage A'BC' about point B yields

$$M_B + M_{C'} - T\, l_{AB} + m\, g\, l_{AB} \sin\left(\alpha_1\right)$$
$$+\ F_{C'D'}\, l_{BC} \cos\left(\frac{\pi}{2} - \theta_{BC'D'}\right) = 0,\quad (A9)$$

while doing the same for linkage D'EF' gives

$$M_E + M_{D'} - F_{C'D'}\, l_{DE} \cos\left(\frac{\pi}{2} - \theta_{C'D'E}\right) = 0.\quad (A10)$$

Solving Eq. (A10) for $F_{C'D'}$, substituting that result into Eq. (A9) and rearranging yields:

$$T = \left(M_B + M_{C'}\right)/l_{AB} + m\, g \sin\left(\alpha_1\right)$$
$$+\ \frac{\left(M_E + M_{D'}\right) l_{BC} \cos\left(\frac{\pi}{2} - \theta_{BC'D'}\right)}{l_{AB}\, l_{DE} \cos\left(\frac{\pi}{2} - \theta_{C'D'E}\right)}\ (A11)$$

which is the same equation given in Eq. (2). The moments in Eq. (A11) are

$$M_B = \alpha_1\, k_B,\qquad M_{C'} = \left(\theta_{BC'D'} - \theta_{BCD}\right) k_{C'}$$
$$M_E = \alpha_2\, k_E,\qquad M_{D'} = \left(\theta_{C'D'E} - \theta_{CDE}\right) k_{D}\, ^{(A12)}$$

where the k values represent the different torsional spring constants at each position. From the deflection analysis of the previous section, all the angles in Eqs. (A11) and (A12) can be computed given an initial deflection $d_{AA'}$ (or more simply by choosing a value of α_1).

[1] Y. Lee, G.N. Kudva, and T.A. Litzinger. "A facility for solid-propellant response measurements under pressure-driven conditions". *Meas. Sci. Technol.*, **11**(1), 2000.

[2] K.D. Diamant and R.B. Cohen. "High power microwave electrothermal thruster performance on water". 38th AIAA/ASME/SE/ASEE Joint Propulsion Conference, July 7-10, 2002. AIAA Paper 2002-3662.

[3] K.D. Diamant, J.E. Brandenburg, R.B. Cohen, and J.F. Kline. "Performance measurements of a water fed microwave electrothermal thruster". 37th AIAA/ASME/SE/ASEE Joint Propulsion Conference, July 8-11, 2001. AIAA Paper 2001-3900.

[4] F. Paganucci, P. Rossetti, and M. Andrenucci. "Performance of an applied field MPD thruster with a pre-ionization chamber". 33rd AIAA Plasmadynamics and Lasers Conference, May 20-23, 2002. AIAA Paper 2002-2103.

[5] T.W. Haag. "Thrust stand for high-power electric propulsion devices". *Rev. Sci. Instrum.*, **62**(5), 1991.

[6] L.D. Cassady, A.D. Kodys, and E.Y. Choueiri. "A thrust stand for high-power steady-state plasma thrusters".

[7] M.A. Cappelli, Q.E. Walker, and N.B. Meezan. "Performance of a linear Hall discharge with an open electron drift". 37th AIAA/ASME/SE/ASEE Joint Propulsion Conference, July 8-11, 2001. AIAA Paper 2001-3503.

[8] D. Manzella, R. Jankovsky, and R. Hofer. "Laboratory model 50 kW Hall thruster". 38th AIAA/ASME/SE/ASEE Joint Propulsion Conference, July 7-10, 2002. AIAA Paper 2002-3676.

[9] A. Smirnov, Y. Raitses, and N.J. Fisch. "Performance studies of miniaturized cylindrical and annular Hall thrusters". 38th AIAA/ASME/SE/ASEE Joint Propulsion Conference, July 7-10, 2002. AIAA Paper 2002-3823.

[10] E.A. Cubbin, J.K. Ziemer, E.Y. Choueiri, and R.G. Jahn. "Pulsed thrust measurements using laser interferometry". *Rev. Sci. Instrum.*, **68**(6), 1997.

[11] A. Sasoh and Y. Arakawa. "A high-resolution thrust stand for ground tests of low-thrust space propulsion devices". *Rev. Sci. Instrum.*, **64**(3), 1993.

[12] A.D. Ketsdever and E.P. Muntz. "Facility effects on

performance measurements of micropropulsion systems". 37th AIAA/ASME/SE/ASEE Joint Propulsion Conference, July 8-11, 2001. AIAA Paper 2001-3335.

[13] A.D. Ketsdever, A.A. Green, and E.P. Muntz. "Momentum flux measurements from under expanded orifices: Applications for microspacecraft systems". 39th AIAA Aerospace Sciences Meeting, Jan. 8-11, 2001. AIAA Paper 2001-0502.

[14] B. Reed. "Decomposing solid micropropulsion nozzle performance issues". 31st AIAA Aerospace Sciences Meeting, Jan. 6-9, 2003. AIAA Paper 2003-0672.

[15] W.D. Willis III, C.M. Zakrzwski, and S.M. Merkowitz. "Development of a thrust stand to meet LISA mission requirements". 38th AIAA/ASME/SE/ASEE Joint Propulsion Conference, July 7-10, 2002. AIAA Paper 2002-3820.

[16] J.K. Ziemer. "Laser ablation microthruster technology". 33rd AIAA Plasmadynamics and Lasers Conference, May 20-23, 2002. AIAA Paper 2002-2153.

[17] T.W. Haag. "PPT thrust stand". 31st AIAA/ASME/SE/ASEE Joint Propulsion Conference, July 10-12, 1995. AIAA Paper 95-2917.

[18] K.W. Stark, T. Dennis, D. McHugh, and T. Williams. "Design and development of a micropound extended range thrsut stand". Technical Report NASA TN D-7029, Aug. 1971.

[19] T.W. Haag. "Thrust stand for pulsed plasma thrusters". *Rev. Sci. Instrum.*, **68**(5), 1997.

[20] T.E. Markusic, K.A. Polzin, E.Y. Choueiri, M. Keidar, I.D. Boyd, and N. Lepsetz. "Ablative Z-pinch pulsed plasma thruster". *J. Propuls. Power*, **21**(3):392–400, 2005.

[21] T.E. Markusic, J.E. Jones, and M.D. Cox. "Thrust stand for electric propulsion performance evaluation". In 40th *AIAA/ASME/SAE/ASEE Joint Propulsion Conference*, Ft. Lauderdale, FL, July 11-14, 2004. AIAA 2004-3441.

[22] Y. Raitses and N.J. Fisch. "Parametric investigations of a nonconventional hall thruster". *Phys. Plasmas*, **8**(5):2579, May 2001.

[23] A. Smirnov, Y. Raitses, and N.J. Fisch. "Parametric investigations of a miniaturized cylindrical and annular hall thrusters". *J. Appl. Phys.*, **92**(10):5673, Nov. 2002.

[24] A. Smirnov, Y. Raitses, and N.J. Fisch. "Enhanced ionization in the cylindrical hall thruster". *J. Appl. Phys.*, **94**(2):852, July 2003.

[25] A. Smirnov, Y. Raitses, and N.J. Fisch. "Plasma measurements in a 100 w cylindrical hall thruster". *J. Appl. Phys.*, **95**(5):2283, Mar. 2004.

[26] A. Smirnov, Y. Raitses, and N.J. Fisch. "Electron cross-field transport in a low power cylindrical hall thruster". *Phys. Plasmas*, **11**(1):4922, Nov. 2004.

[27] D. York, N.M. Evensen, M.L. Martinez, and J.D.B. Delgado. "Unified equations for the slope, intercept, and standard errors of the best straight line". *Am. J. Phys.*, **72**(3):367, Mar. 2004.

[28] A. Smirnov, Y. Raitses, and N.J. Fisch. "The effect of magnetic field on the performance of low-power cylindrical Hall thrusters". 29th International Electric Propulsion Conference, Oct. 31 - Nov. 4, 2005. IEPC Paper 2005-099.